Chaos, Solitons and Fractals 205 (2026) 117884

Contents lists available at ScienceDirect

Chaos, Solitons and Fractals

journal homepage: www.elsevier.com/locate/chaos

On the behavior of Linear Dependence, Smaller, and Generalized Alignment Indices in discrete and continuous chaotic systems

Matheus Rolim Sales [a,b], Edson Denis Leonel [b], Chris G. Antonopoulos [a,*]

[a] University of Essex, School of Mathematics, Statistics and Actuarial Science, CO4 3SQ, Wivenhoe Park, Colchester, United Kingdom
[b] São Paulo State University (UNESP), Institute of Geosciences and Exact Sciences, 13506-900, Rio Claro, SP, Brazil

ARTICLE INFO

Keywords:
Linear Dependence Index (LDI)
Smaller Alignment Index (SALI)
Generalized Alignment Index (GALI)
Discrete-time systems
Continuous-time systems
Lyapunov exponents

ABSTRACT

The discrimination between order and chaos in dynamical systems remains a central problem in the field. Among the most widely used indicators are the Smaller Alignment Index (SALI), the Generalized Alignment Index (GALI), and the Linear Dependence Index (LDI), all of which exploit the evolution of deviation vectors to distinguish regular from chaotic motion. In this paper, we first show analytically, and confirm numerically, that the decay rates of LDI for chaotic orbits in both discrete- and continuous-time systems are the same with those of GALI reported in the literature. Our derivations, however, are more accessible, relying on the Singular Value Decomposition rather than the wedge-product formulation of GALI, which involves volumes of higher-dimensional parallelepipeds. We then derive the analytical expression for the decay rate of SALI in chaotic maps, demonstrating that it depends on the difference of the two largest Lyapunov exponents, as previously established for continuous-time systems. Crucially, we show analytically that the second Lyapunov exponent must always be considered, independent of its sign, in order to capture correctly the decay of SALI. This contrasts with existing results for continuous systems, where the second exponent is greater or equal than zero for chaotic orbits. Our analytical and numerical findings, therefore, extend the SALI decay rate formula to both continuous- and discrete-time systems. Finally, we confirm numerically that the decay rate of the SALI for chaotic maps is accurately described by our formula, which incorporates the two largest Lyapunov exponents, regardless of whether the second exponent is positive, zero, or negative.

1. Introduction

In his seminal work in 1963, Lorenz provided the first numerical evidence of deterministic chaos (or simply chaos) by demonstrating the existence of a strange attractor: an aperiodic, deterministic set that is highly sensitive to small changes in the initial conditions [1]. Since then, the detection and characterization of chaos in dynamical systems, along with the development of reliable theoretical and numerical methods, have become a central problem in modern research. A key tool in this context is the computation of the Lyapunov exponents (LEs) [2–5], which quantify the average exponential rates of divergence or convergence of nearby orbits in phase space. Lyapunov exponents provide the foundation for distinguishing between regular and chaotic dynamics: an orbit with at least one positive exponent is said to be chaotic.

However, the computation of all or a subset of LEs can be time-consuming and numerically demanding, particularly for high-dimensional systems. This has motivated the introduction of several alternative chaos indicators, each with its own advantages.

* Corresponding author.
E-mail addresses: rolim.sales.m@gmail.com (M.R. Sales), edson-denis.leonel@unesp.br (E.D. Leonel), canton@essex.ac.uk (C.G. Antonopoulos).

https://doi.org/10.1016/j.chaos.2026.117884
Received 3 September 2025; Received in revised form 6 November 2025; Accepted 5 January 2026
Available online 9 January 2026

Among those closely related to LEs are the fast Lyapunov indicator (FLI) [6–8], the relative Lyapunov indicator (RLI) [9,10], and the mean exponential growth factor of nearby orbits (MEGNO) [11,12]. These methods share the same conceptual basis as the traditional LE approach, but typically converge faster and require less computational effort. Additionally, other approaches have been developed based on time series analysis, such as the "0–1" test [13], the finite-time rotation number [14], the weighted Birkhoff average method [15–23], and various recurrence quantification techniques [24–31].

Among the most successful and rapidly converging modern methods are the Smaller Alignment Index (SALI) [32–34], its generalization, the Generalized Alignment Index (GALI) [35–39], and the Linear Dependence Index (LDI) [40]. These methods are based on the evolution of multiple deviation vectors along an orbit and exploit their tendency to collapse onto the most unstable directions in tangent spaces. SALI, which relies on only two deviation vectors, provides a fast distinction between regular and chaotic motion. GALI extends this idea to multiple vectors, providing a deeper understanding of the geometry of regular and chaotic motion. LDI, on the other hand, reformulates GALI using tools from linear algebra, focusing on the linear dependence of deviation vectors, exploiting the Singular Value Decomposition (SVD) method.

While these indices have successfully been applied to both continuous-time Hamiltonian and dissipative [41] systems, a systematic analysis of their decay rates, both analytically and numerically, has not been done in the case of chaotic discrete-time systems, i.e., chaotic maps. Therefore, in this paper, we derive the decay rate of LDI for chaotic maps using the SVD of the matrix of deviation vectors. This linear-algebraic formulation provides a more direct and transparent route compared to the wedge-product interpretation used for GALI [35]. Through this approach, we show that the decay rate of LDI coincides with the decay rate previously reported for GALI. We then derive an analytical expression for the decay rate of SALI for chaotic maps and show it depends on the difference of the two largest Lyapunov exponents, as in the case of continuous-time systems reported in the literature [34,38]. However, our derivations show that the exponent of the decay rate of SALI is given by the difference of the first two LEs, regardless of whether the second LE is positive, zero, or negative. This is different to what is reported in the literature for continuous systems [34,38], where the second Lyapunov exponent can only be positive or zero for chaotic orbits [3,4,42], meaning that the exponent of the decay rate is given by the maximum LE if the second is zero. Thus, our analytical and numerical results generalize the decay rate formula of SALI for both continuous- and discrete-time chaotic systems.

The paper is organized as follows: In Section 2 we derive the analytical expression for the decay rate of LDI using the SVD method instead of the method in Ref. [35], and in Section 3, we validate these results for three- and ten-dimensional maps as well as for a Hamiltonian system. In Section 4, we revisit the analytical derivation of SALI and derive analytically a generalized expression for both discrete- and continuous-time systems, which we validate through numerical simulations on two paradigmatic maps: the Arnold's cat map and the dissipative baker map. Section 5 contains our final remarks and thoughts. In the Appendix, we discuss the computation performance of the LDI $_k$ indicator using the SVD procedure and compare with the Lyapunov exponents calculation.

2. Analytical derivation of the decay rates of the Linear Dependence Index for chaotic trajectories of discrete systems

Let $\boldsymbol{\Phi}^n(\mathbf{x}_0)$ be a discrete-time dynamical system in $\mathbb{R}^d$ and $D\boldsymbol{\Phi}^n(\mathbf{x}_0)$ be the nth iterate of the Jacobian matrix of the system. The Lyapunov spectrum $\lambda_1 > \lambda_2 > \cdots > \lambda_d$ can be defined using Oseledec's multiplicative theorem [43]. The theorem states that for almost every initial condition $\mathbf{x}_0 \in \mathbb{R}^d$, the following limit exists

$$M(\mathbf{x}_0) = \lim_{n\to\infty} \left\{ \left[D\boldsymbol{\Phi}^n(\mathbf{x}_0)\right]^T D\boldsymbol{\Phi}^n(\mathbf{x}_0) \right\}^{1/2n},$$

and the LEs are related to the eigenvalues of the limiting matrix M as

$$\lambda_i = \lim_{n\to\infty} \frac{1}{n} \ln \left\| D\boldsymbol{\Phi}^n(\mathbf{x}_0)\hat{\mathbf{w}}_i \right\|,$$

where $\hat{\mathbf{w}}_i$ is the corresponding eigenvector of M. A general deviation vector can then be expressed in the basis $\{\hat{\mathbf{w}}_i\}$ as

$$\mathbf{d}(n) = \sum_{i=1}^{d} c_i e^{\lambda_i n} \hat{\mathbf{w}}_i. \tag{1}$$

Let now $A(n) \in \mathbb{R}^{d\times k}$ be a matrix whose columns are $k \le d$ linearly independent deviation vectors evolved in time, under the linearized dynamics, i.e.,

$$A(n) = D\boldsymbol{\Phi}^n(\mathbf{x}_0)A(0), \tag{2}$$

where $A(0) \in \mathbb{R}^{d\times k}$ is the matrix of k linearly independent initial deviation vectors. For chaotic orbits, as the number of iterations n increases, the matrix A becomes dominated by the direction of maximal growth, i.e., all deviation vectors align with the most unstable direction, making it impossible to determine the smaller LEs. That is a classical issue in numerical simulations of dynamical systems, and several methods have been proposed to solve it [2–5], with the successive QR factorization of A or use of the Gram–Schmidt method being the most traditional ones. While these methods avoid this alignment, the SALI and GALI methods exploit it.

SALI is a quantity that checks whether two normalized deviation vectors

$$\hat{\mathbf{d}}_1 = \frac{\mathbf{d}_1}{\|\mathbf{d}_1\|},$$
$$\hat{\mathbf{d}}_2 = \frac{\mathbf{d}_2}{\|\mathbf{d}_2\|},$$

become linearly dependent, i.e., whether they fall in the same direction (parallel or anti-parallel), and is defined by

$$\mathrm{SALI}(n) = \min\left\{\left\|\hat{\mathbf{d}}_1 - \hat{\mathbf{d}}_2\right\|, \left\|\hat{\mathbf{d}}_1 + \hat{\mathbf{d}}_2\right\|\right\}, \tag{3}$$

where $\mathbf{d}_1$ and $\mathbf{d}_2$ are evolved according to Eq. (2). Hence, SALI is given by the minimum of the two quantities in the curly brackets at any iteration n. This is equivalent to measuring the area of the parallelogram formed by these two vectors: As they fall in the same direction, the area goes to zero.

The GALI method generalizes this idea by considering k normalized deviation vectors, $\hat{\mathbf{d}}_k$ and measuring the volume of the k-dimensional parallelepiped formed by them. It is defined as the norm of the wedge product (denoted $\wedge$) of the k normalized deviation vectors $\hat{\mathbf{d}}_k$

$$\mathrm{GALI}_k(n) = \left\|\hat{\mathbf{d}}_1 \wedge \hat{\mathbf{d}}_2 \wedge \cdots \wedge \hat{\mathbf{d}}_k\right\|. \tag{4}$$

It has been shown that both SALI and GALI accurately distinguish between regular and chaotic motion [32–34,34–37,41]. Moreover, the authors in [36] demonstrated that GALI can be used to identify the dimensionality of the space of regular motion. However, the analytical derivation of the relation between GALI and the LEs, given in Ref. [35], is cumbersome. Antonopoulos et al. [40] demonstrated numerically that the product of the k singular values of A is proportional to GALI_k. Hence, they defined LDI of order k as

$$\mathrm{LDI}_k(n) = \prod_{i=1}^{k} \sigma_i, \tag{5}$$

where σ_i are the singular values of A obtained from its SVD

$$A = U\Sigma V^T, \tag{6}$$

where $U \in \mathbb{R}^{d\times d}$ is an orthogonal matrix whose columns are the left singular vectors, $\Sigma \in \mathbb{R}^{d\times k}$ is a diagonal matrix containing the non-negative singular values, i.e., $\sigma_i = \Sigma_{ii}$, and $V \in \mathbb{R}^{k\times k}$ is an orthogonal matrix whose columns are the right singular vectors.

Next, we show analytically that

$$\mathrm{LDI}_k \equiv \mathrm{GALI}_k,$$

for all k indices, that is for $k \in [2, d]$, corroborating the numerical results in [40]. We start with the Gram matrix $G = A^T A \in \mathbb{R}^{k\times k}$, with entries $G_{ij} = \hat{\mathbf{d}}_i \cdot \hat{\mathbf{d}}_j$. The wedge product of the k vectors, $\hat{\mathbf{d}}_1, \hat{\mathbf{d}}_2, \ldots, \hat{\mathbf{d}}_k$ is related to the determinant of the Gram matrix by

$$\left\|\hat{\mathbf{d}}_1 \wedge \hat{\mathbf{d}}_2 \wedge \ldots \hat{\mathbf{d}}_k\right\|^2 = \det(G).$$

The Gram matrix is written in terms of the SVD of A (see Eq. (6)) as

$$G = \left(U\Sigma V^T\right)^T U\Sigma V^T = V(\Sigma^T\Sigma)V^T.$$

Since V is an orthogonal matrix, this relation is a similarity transformation, i.e., matrix G is similar to matrix $\Sigma^T\Sigma$, and thus they share the same eigenvalues, and, consequently, the same determinant:

$$\det(G) = \det\left(\Sigma^T\Sigma\right) = \prod_{i=1}^{k} \sigma_i^2.$$

Therefore, since $\mathrm{GALI}_k = \sqrt{\det(G)}$, we find that

$$\mathrm{GALI}_k \equiv \mathrm{LDI}_k = \prod_{i=1}^{k} \sigma_i. \tag{7}$$

The next step is to relate the singular values σ_i to the LEs λ_i. To this end, we rewrite matrix $A(n)$ in terms of the $\{\hat{\mathbf{w}}_i\}$ basis as

$$A(n) = \sum_{i=1}^{d} e^{\lambda_i n}\hat{\mathbf{w}}_i \mathbf{C}_i^T, \tag{8}$$

where $\mathbf{C}_i \in \mathbb{R}^k$ contains the coefficients of the projections of the initial deviation vectors onto the $\hat{\mathbf{w}}_i$ direction. By defining the following matrices

$$C = [\mathbf{C}_1 \ \ldots \ \mathbf{C}_d] \in \mathbb{R}^{k\times d},$$
$$W = [\hat{\mathbf{w}}_1 \ \ldots \ \hat{\mathbf{w}}_d] \in \mathbb{R}^{d\times d},$$
$$D = \mathrm{diag}(e^{\lambda_1 n}, \ldots, e^{\lambda_d n}) \in \mathbb{R}^{d\times d},$$

we can rewrite Eq. (8) as

$$A(n) = WDC^T. \tag{9}$$

It is important to mention that, in general, the columns $\mathbf{C}_i$ are linearly independent but not orthogonal or normalized. Nevertheless, we can perform a QR factorization of C, and write $C = QR$, with $Q \in \mathbb{R}^{k\times k}$ orthogonal and $R \in \mathbb{R}^{k\times d}$ upper triangular with positive diagonal. Substituting into Eq. (9) gives

$$A(n) = WDR^TQ^T. \tag{10}$$

Since W and Q are orthogonal, the singular values of A are those of the matrix $B = DR^T$. We know that the eigenvalues of $B^T B$ (or BB^T) give the σ_i^2, where σ_i are the singular values of B and, consequently, of A. Thus

$$B^T B = RD^2 R^T,$$

where $D^2 = \mathrm{diag}(e^{2\lambda_1 n}, e^{2\lambda_2 n}, \ldots, e^{2\lambda_d n})$. Let $\mathbf{r}_j \in \mathbb{R}^k$ denote the jth column of R^T (or equivalently, the jth row of R). Then

$$RD^2 R^T = \sum_{j=1}^{d} e^{2\lambda_j n} \mathbf{r}_j \mathbf{r}_j^T. \tag{11}$$

We can factor out $e^{2\lambda_1 n}$ in Eq. (11) and write

$$B^T B = e^{2\lambda_1 n}\left(\mathbf{r}_1\mathbf{r}_1^T + \sum_{j=2}^{d} e^{2(\lambda_j-\lambda_1)n}\mathbf{r}_j\mathbf{r}_j^T\right) = e^{2\lambda_1 n}\big(M_1 + E_1\big),$$

where $M_1 = \mathbf{r}_1\mathbf{r}_1^T$ is a rank-1 matrix and $E_1 = \sum_{j=2}^{d} e^{2(\lambda_j-\lambda_1)n}\mathbf{r}_j\mathbf{r}_j^T$. Since $\lambda_j < \lambda_1$, E_1 is exponentially small compared to M_1 for large n. Therefore, we can interpret the matrix $M_1 + E_1$ as a perturbation of M_1. This allows us to apply first-order matrix perturbation theory [44] to determine how the largest eigenvalue, $\mu_{\max}$, and hence the leading singular value, deviates from that of M_1. In our case, the first-order perturbation theory gives

$$\mu_{\max}(M_1 + E_1) = \|\mathbf{r}_1\|^2 + \left(\frac{\mathbf{r}_1}{\|\mathbf{r}_1\|}\right)^T E_1 \left(\frac{\mathbf{r}_1}{\|\mathbf{r}_1\|}\right) + \mathcal{O}(\|E_1\|^2).$$

Since $\|E_1\| \propto e^{2(\lambda_2-\lambda_1)n}$, we get

$$\mu_{\max}(M_1 + E_1) = \|\mathbf{r}_1\|^2 + \mathcal{O}(e^{2(\lambda_2-\lambda_1)n}),$$

which leads to

$$\mu_{\max}(B^T B) = \sigma_1^2 = \|\mathbf{r}_1\|^2 e^{2\lambda_1 n}$$

for large n.

For the second largest eigenvalue, we project matrix $B^T B$ onto the subspace orthogonal to $\hat{\mathbf{r}}_1$ by defining $P_1^{\perp} = I - \hat{\mathbf{r}}_1\hat{\mathbf{r}}_1^T$ and writing

$$B_2^T B_2 = P_1^{\perp} B_T B P_1^{\perp} = \sum_{j=2}^{d} e^{2\lambda_j n} P_1^{\perp}\mathbf{r}_j\mathbf{r}_j^T P_1^{\perp},$$

so that the influence of $\mathbf{r}_1$ is removed. We factor the largest remaining LE out

$$B_2^T B_2 = e^{2\lambda_2 n}\left(P_1^{\perp}\mathbf{r}_2\mathbf{r}_2^T P_1^{\perp} + \sum_{j=3}^{d} e^{2(\lambda_j-\lambda_2)n} P_1^{\perp}\mathbf{r}_j\mathbf{r}_j^T P_1^{\perp}\right) = e^{2\lambda_2 n}\big(M_2 + E_2\big),$$

where $M_2 = P_1^{\perp}\mathbf{r}_2\mathbf{r}_2^T P_1^{\perp}$ is rank-1 matrix in the projected subspace and $E_2 = \sum_{j=3}^{d} e^{2(\lambda_j-\lambda_2)n} P_1^{\perp}\mathbf{r}_j\mathbf{r}_j^T P_1^{\perp}$ is exponentially small for large n, that is

$$\|E_2\| \propto e^{2(\lambda_3-\lambda_2)n} \to 0,$$

as $n \to \infty$. The first-order perturbation theory leads to

$$\mu_2(B^T B) = \sigma_2^2 = \left\|P_1^{\perp}\mathbf{r}_2\right\|^2 e^{2\lambda_2 n}.$$

For the ith eigenvalue, μ_i, we define the projection onto the subspace orthogonal to all previously computed singular vectors $\hat{\mathbf{r}}_1, \hat{\mathbf{r}}_2, \ldots, \hat{\mathbf{r}}_{i-1}$

$$P_{i-1}^{\perp} = I - \sum_{m=1}^{i-1} \hat{\mathbf{r}}_m \hat{\mathbf{r}}_m^T$$

and restrict matrix $B^T B$ to that subspace

$$B_i^T B_i = P_{i-1}^{\perp} B^T B P_{i-1}^{\perp} = e^{2\lambda_i n}\big(M_i + E_i\big), \tag{12}$$

where $M_i = P_{i-1}^{\perp}\mathbf{r}_i\mathbf{r}_i^T P_{i-1}^{\perp}$ is a rank-1 matrix in the projected subspace and $\|E_i\| \propto e^{2(\lambda_{i+1}-\lambda_i)n} \to 0$ as $n \to \infty$. This application removes the influence of all previously computed directions. Therefore, the ith singular value of $B = DR^T$, and consequently of A, is

$$\sigma_i = \left\|P_{i-1}^{\perp}\mathbf{r}_i\right\| e^{\lambda_i n},$$

with $i = 1, 2, \ldots, k$.

Assuming chaotic dynamics, numerically, this process might lead to extremely large deviation vectors as $\mathbf{d}(n)$ grows exponentially (see Eq. (1)). Instead, let us repeat this process for the normalized deviation vectors $\hat{\mathbf{d}}$. The norm of the general deviation vector is

$$\|\mathbf{d}(n)\| = \left(\sum_{i=1}^{d} c_i^2 e^{2\lambda_i n}\right)^{1/2}.$$

We can factorize the last equation with respect to $c_1^2 e^{2\lambda_1 n}$, leading us to

$$\begin{aligned}\|\mathbf{d}(n)\| &= \left[c_1^2 e^{2\lambda_1 n}\left(1 + \sum_{i=2}^{d} \frac{c_i^2}{c_1^2} e^{-2(\lambda_1-\lambda_i)n}\right)\right]^{1/2}, \\ &= |c_1| e^{\lambda_1 n}\left(1 + \sum_{i=2}^{d} \frac{c_i^2}{c_1^2} e^{-2(\lambda_1-\lambda_i)n}\right)^{1/2}.\end{aligned}$$

The quantity inside the brackets in the last equation goes to 1 as n increases. Therefore, the norm of $\mathbf{d}$ is simply

$$\|\mathbf{d}(n)\| = |c_1| e^{\lambda_1 n}.$$

Thus, the normalized deviation vector is

$$\hat{\mathbf{d}}(n) = \frac{\mathbf{d}(n)}{\|\mathbf{d}(n)\|} = \mathrm{sgn}(c_1)\hat{\mathbf{w}}_1 + \sum_{i=2}^{d} \frac{c_i}{|c_1|} e^{-(\lambda_1-\lambda_i)n}\hat{\mathbf{w}}_i. \tag{13}$$

Let $\tilde{A}(n) \in \mathbb{R}^{d\times k}$ be the matrix whose columns are these normalized vectors. In the $\{\hat{\mathbf{w}}_i\}$ basis, it takes the form

$$\tilde{A}(n) = \|\mathbf{s}\|\hat{\mathbf{w}}_1\left(\frac{\mathbf{s}}{\|\mathbf{s}\|}\right)^T + \sum_{i=2}^{d} \|\tilde{\mathbf{C}}_i\| e^{-(\lambda_1-\lambda_i)n}\hat{\mathbf{w}}_i\left(\frac{\tilde{\mathbf{C}}_i}{\|\tilde{\mathbf{C}}_i\|}\right)^T, \tag{14}$$

where $\mathbf{s} \in \mathbb{R}^k$ has entries $s_j = \mathrm{sgn}(c_1^{(j)})$, and $\tilde{\mathbf{C}}_i \in \mathbb{R}^k$ collects the relative coefficients $\tilde{C}_i^{(j)} = c_i^{(j)}/|c_1^{(j)}|$. We can express this in a compact matrix-product form, analogous to the non-normalized case (see Eq. (9)) as

$$\tilde{A}(n) = W\tilde{D}\tilde{C}^T, \tag{15}$$

where

$$\begin{aligned}&\tilde{C} = [\hat{\mathbf{s}}, \hat{\tilde{\mathbf{C}}}_2, \ldots, \hat{\tilde{\mathbf{C}}}_d]^T \in \mathbb{R}^{k\times d}, \\ &W = [\hat{\mathbf{w}}_1 \ \cdots \ \hat{\mathbf{w}}_d] \in \mathbb{R}^{d\times d}, \\ &\tilde{D} = \mathrm{diag}\left(\sqrt{k}, e^{-(\lambda_1-\lambda_2)n}, \ldots, e^{-(\lambda_1-\lambda_d)n}\right) \in \mathbb{R}^{d\times d}.\end{aligned}$$

Substituting the QR factorization $\tilde{C} = \tilde{Q}\tilde{R}$, where $\tilde{Q} \in \mathbb{R}^{k\times k}$ and $\tilde{R} \in \mathbb{R}^{k\times d}$ into Eq. (15) yields

$$\tilde{A}(n) = W\tilde{D}\tilde{R}^T\tilde{Q}^T. \tag{16}$$

As in the non-normalized case, the singular values of $\tilde{A}$ are the singular values of $\tilde{B} = \tilde{D}\tilde{R}^T$, i.e., the square roots of the eigenvalues of

$$\tilde{B}^T\tilde{B} = \tilde{R}\tilde{D}^2\tilde{R}^T = k\,\tilde{\mathbf{r}}_1\tilde{\mathbf{r}}_1^T + \sum_{j=2}^{d} e^{-2(\lambda_1-\lambda_j)n}\tilde{\mathbf{r}}_j\tilde{\mathbf{r}}_j^T, \tag{17}$$

where $\tilde{\mathbf{r}}_j \in \mathbb{R}^k$ denotes the jth column of $\tilde{R}^T$. Eq. (17) is already in the form of a rank-1 matrix plus an exponentially small matrix. Applying first-order perturbation theory gives the largest eigenvalue

$$\mu_{\max}(\tilde{B}^T\tilde{B}) = \left\|\tilde{\mathbf{r}}_1\right\|^2 k.$$

For the remaining eigenvalues ($2 \le i \le k$), we can define the projection onto the subspace orthogonal to vectors $\{\tilde{\mathbf{r}}_1, \tilde{\mathbf{r}}_2, \ldots, \tilde{\mathbf{r}}_{i-1}\}$ as

$$\tilde{P}_i^{\perp} = I - \sum_{m=1}^{i-1} \hat{\tilde{\mathbf{r}}}_m\hat{\tilde{\mathbf{r}}}_m^T$$

and restrict the matrix $\tilde{B}^T\tilde{B}$ to this subspace

$$\tilde{B}_i^T\tilde{B}_i = \tilde{P}_{i-1}^{\perp}\tilde{B}^T\tilde{B}\tilde{P}_{i-1}^{\perp} = e^{-2(\lambda_1-\lambda_i)n}\left(\tilde{P}_{i-1}^{\perp}\tilde{\mathbf{r}}_i\tilde{\mathbf{r}}_i^T\tilde{P}_{i-1}^{\perp} + \sum_{j=i+1}^{d} e^{-2(\lambda_j-\lambda_i)n}\tilde{P}_{j-1}^{\perp}\tilde{\mathbf{r}}_j\tilde{\mathbf{r}}_j^T\tilde{P}_{j-1}^{\perp}\right).$$

This corresponds to an exponentially small perturbation of a rank-1 matrix in the projected subspace (see Eq. (12)). Thus, for large n, the ith eigenvalue of $\tilde{B}_i^T\tilde{B}_i$ at first-order is

$$\mu_i(\tilde{B}_i^T\tilde{B}_i) = \left\|\tilde{P}_{i-1}^{\perp}\tilde{\mathbf{r}}_i\right\|^2 e^{-2(\lambda_1-\lambda_i)n}.$$

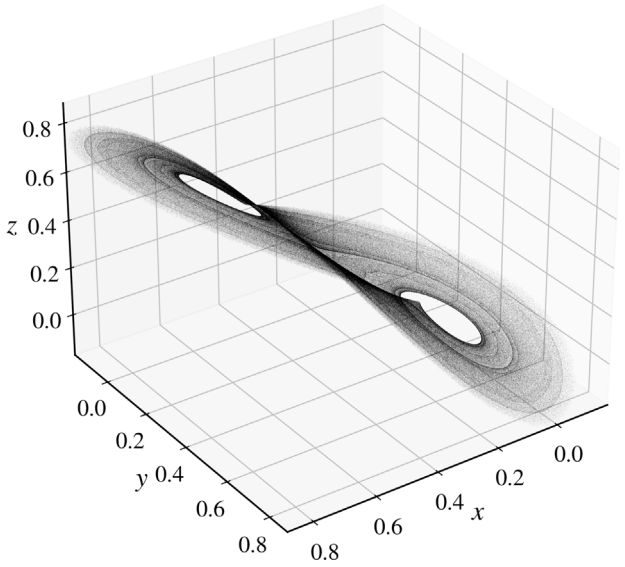

Fig. 1. The attractor of the three-dimensional Hénon map of Eq. (20) with parameters $(M_1, M_2, B) = (0.0, 0.85, 0.7)$.

Finally, the asymptotic behavior of the singular values of $\tilde{A}$ are

$$\begin{aligned} \sigma_1 &\propto \sqrt{k}, \\ \sigma_i &\propto e^{-(\lambda_1-\lambda_i)n}, \end{aligned} \tag{18}$$

for $2 \leq i \leq k$.

The main difference between the singular values of the normalized deviation matrix and the non-normalized ones is that the largest singular value is now bounded instead of growing exponentially for chaotic orbits. The remaining singular values decay exponentially with rates given by $(\lambda_1 - \lambda_i)$ and LDI, and GALI (see Eq. (7)), is the product of all singular values

$$\mathrm{LDI}_k = \prod_{i=1}^{k} \sigma_i \propto e^{-[(\lambda_1-\lambda_2)+(\lambda_1-\lambda_3)+\cdots+(\lambda_1-\lambda_k)]n} = e^{-[(k-1)\lambda_1-\lambda_2-\lambda_3-\cdots-\lambda_k]n}. \tag{19}$$

This expression is the same as the one in [35] for GALI_k with the advantage of having been derived here using easier analytical calculations. By that, we mean our analytical derivations are easier to follow as they involve the use of the SVD method instead of wedge products to compute the volume of higher-dimensional parallelepipeds [35].

Both GALI and LDI ultimately quantify the degree of linear dependence of deviation vectors. As these vectors evolve in the tangent space of chaotic dynamics, they progressively align with the most unstable direction, eventually collapsing onto a single direction and becoming linearly dependent. A set of vectors is linearly independent if and only if the determinant of the Gram matrix is nonzero, or equivalently, if all singular values are nonzero. In practice, computing singular values is numerically more stable and reliable than evaluating determinants as the determinants are highly sensitive to rounding-off errors and can easily overflow/underflow [45,46]. In Section 3, we numerically validate our analytical result considering discrete- and continuous-time dynamical systems. The validity of Eq. (19) has already been verified thoroughly for continuous-time systems, both Hamiltonian [35] and dissipative [41], however, to the best of our knowledge, not for discrete-time systems.

3. Numerical verification of the analytical expression for the decay rates of the Linear Dependence Index

All our numerical simulations have been performed using *pynamicalsys* [47], an open-source Python toolkit for the analysis of dynamical systems.

3.1. Discrete-time systems

To test our analytical result for the LDI, Eq. (19), let us first consider a three-dimensional version of the Hénon map $\Phi : \mathbb{R}^3 \to \mathbb{R}^3$, given by the following equations [48]

$$\Phi : \begin{cases} x_{n+1} = y_n, \\ y_{n+1} = z_n, \\ z_{n+1} = M_1 + Bx_n + M_2 y_n - z_n^2. \end{cases} \tag{20}$$

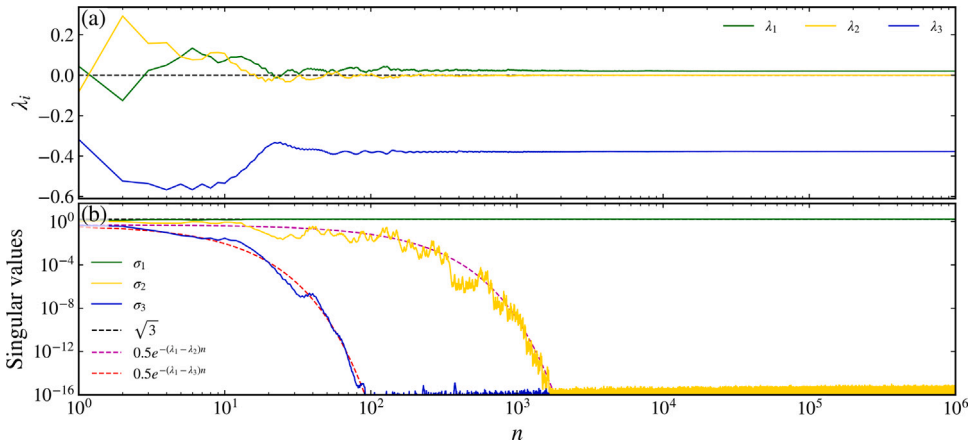

Fig. 2. The time evolution of (a) the LEs and (b) the singular values of the deviation matrix (see Eq. (14)) for the three-dimensional Hénon map (see Eq. (20)) with parameters $(M_1, M_2, B) = (0.0, 0.85, 0.7)$. (For interpretation of the references to color in this figure legend, the reader is referred to the web version of this article.)

This map is one of the generalizations of the paradigmatic two-dimensional Hénon map. Here, $(x, y, z) \in \mathbb{R}^3$ are the state variables and $(M_1, M_2, B) \in \mathbb{R}^3$ are the parameters of the system. The determinant of the Jacobian is constant, $\det(D\Phi) = B$, so the map is dissipative for $B < 1$. In our simulations, we use $M_1 = 0$, $M_2 = 0.85$, $B = 0.7$, a total iteration time of $N = 1.5 \times 10^6$, and discard a transient of 0.5×10^6. Fig. 1 shows the resulting attractor for the initial condition $(x_0, y_0, z_0) = (0.6, 0.2, 0.3)$. This attractor is chaotic, as confirmed by the LEs in Fig. 2(a). Particularly, there are three exponents, with the largest (green curve) being positive, the second (yellow curve) being approximately zero, and the third being negative.

To further verify the relation between the singular values of the deviation matrix and the LEs (see Eq. (18)), we compute the time series of the singular values, shown in Fig. 2(b). The largest singular value, σ_1, rapidly converges to the constant value $\sigma_1 = \sqrt{3}$, while the remaining two singular values (yellow and blue curves) decay exponentially with time. The dashed lines, corresponding to the analytical values predicted by Eq. (18) using the LEs from Fig. 2(a), are in excellent agreement with the numerical results, confirming the validity of our analytical derivation for the singular values.

Having confirmed that the singular values of the deviation matrix follow the analytical predictions, next we compute LDI, defined as the product of these singular values, shown in Eq. (19). We consider an ensemble of 100 initial conditions, randomly chosen within a distance of at most 10^{-3} from $(x_0, y_0, z_0) = (0.6, 0.2, 0.3)$. For each initial condition, we compute LDI_2 in Fig. 3(a), LDI_3 in Fig. 3(b), and perform a best fit for each LDI curve to obtain the corresponding decay rates. This process is repeated for all initial conditions, and the results are averaged to obtain a representative LDI behavior. In the figures, the black dashed curves represent the average of all best-fit curves, while the black dash-dotted curves indicate the mean ± three standard deviations of these fits. For each initial condition in the ensemble, we also compute the LEs and calculate the mean and standard deviation over all 100 initial conditions. These averaged values provide the reference combinations of LEs we use for comparison with the LDI decay rates. The decay rates obtained from the LDI curves are in excellent agreement with these predictions (the single numbers in round brackets denote one standard deviation around the reported number), for example $-0.021(1) = (-0.02, -0.022)$: $\mathrm{LDI}_2 \propto \exp(-0.021(1)n)$ closely matches $\lambda_1 - \lambda_2 = 0.01999(6)$, while $\mathrm{LDI}_3 \propto \exp(-0.42(3)n)$ is consistent with $2\lambda_1 - \lambda_2 - \lambda_3 = 0.4169(2)$. These results confirm that LDI accurately captures the combination of LEs predicted by Eq. (19), thereby validating our analytical derivation for discrete-time chaotic systems.

Next, we test our analytical results for a higher-dimensional discrete-time chaotic system. We consider a network of N identical logistic maps coupled in a ring topology [49]

$$x_{n+1}^{(i)} = f\left(x_n^{(i)}\right) + \frac{\sigma}{2rN} \sum_{j=i-rN}^{i+rN} \left[f\left(x_n^{(j)}\right) - f\left(x_n^{(i)}\right)\right], \tag{21}$$

where $x^{(i)}$ denotes the state of the ith node ($i = 1, 2, \ldots, N$), n is the discrete time step, σ the coupling strength, r the coupling radius, and $f(x)$ is the local map, chosen as the logistic map $f(x) = ax(1 - x)$. We fix the bifurcation parameter at $a = 3.8$, so that the uncoupled dynamics of each node is chaotic. We consider a network of size $N = 10$ nodes, a coupling strength of $\sigma = 0.15$, and a coupling radius of $r = 0.15$. To illustrate the dynamics of the network, we show the space–time evolution of the network in Fig. 4(a). The figure reveals the absence of coherent spatiotemporal patterns, indicating incoherent dynamics consistent with the weak coupling. We also compute the evolution of the LEs, shown in Fig. 4(b). The network exhibits hyperchaotic behavior, with the two largest LEs being positive.

Similarly to the previous system, we compute the LDI for an ensemble of 100 initial conditions, randomly chosen within a distance of 10^{-3} from each other. Since the network is $N = 10$-dimensional, LDI_k can be computed up to $k = 10$. However, LDI_k

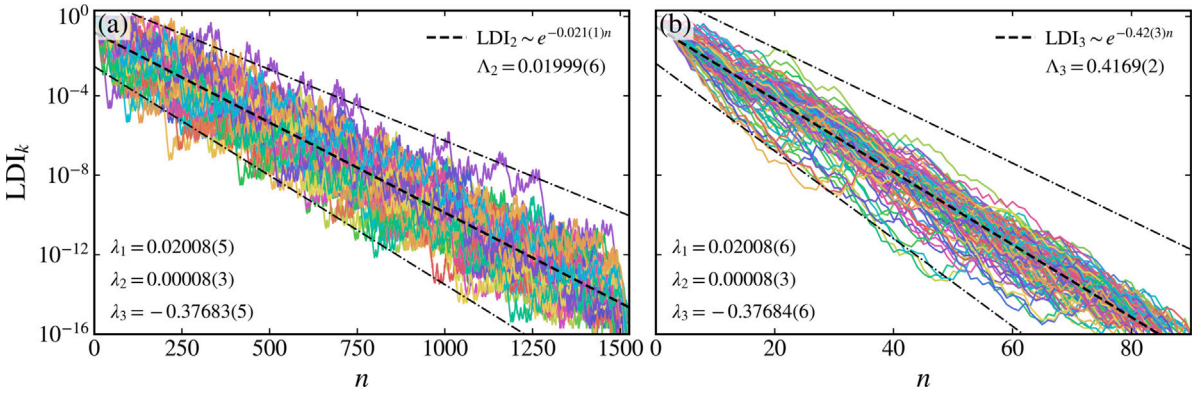

Fig. 3. LDI curves for the three-dimensional Hénon map (see Eq. (20)) with parameters $(M_1, M_2, B) = (0.0, 0.85, 0.7)$. Panels (a) and (b) show LDI_2 and LDI_3, respectively, computed for 100 initial conditions randomly chosen within a distance of at most 10^{-3} from $(x_0, y_0, z_0) = (0.6, 0.2, 0.3)$. The black dashed curves indicate the best-fit average, while the black dash-dotted curves represent the mean ± three standard deviations. (For interpretation of the references to color in this figure legend, the reader is referred to the web version of this article.)

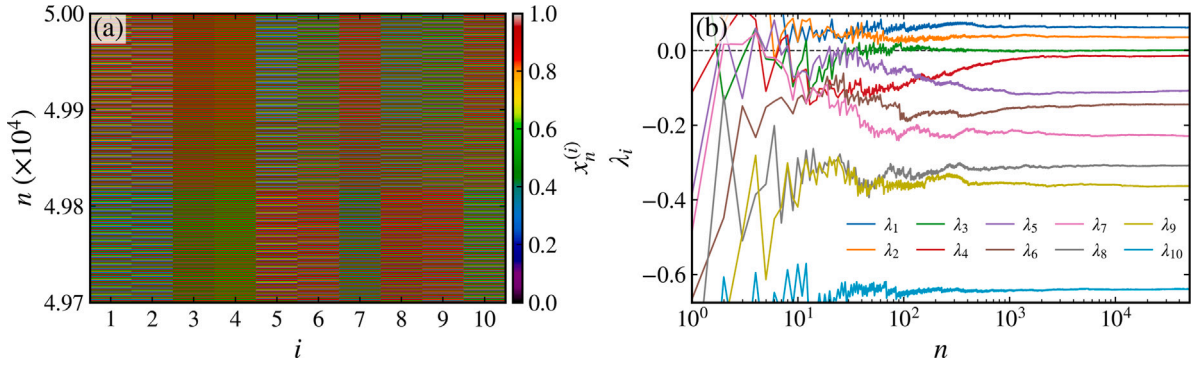

Fig. 4. Spatiotemporal plot and evolution of Lyapunov exponents of system (21): (a) Space–time evolution of a network of $N = 10$ identical logistic maps coupled in a ring topology with coupling strength $\sigma = 0.15$, coupling radius $r = 0.15$, and individual map bifurcation parameter $a = 3.8$. (b) LEs of the network as a function of iteration number. Note that we plot $0.5\lambda_{10}$ for clarity. (For interpretation of the references to color in this figure legend, the reader is referred to the web version of this article.)

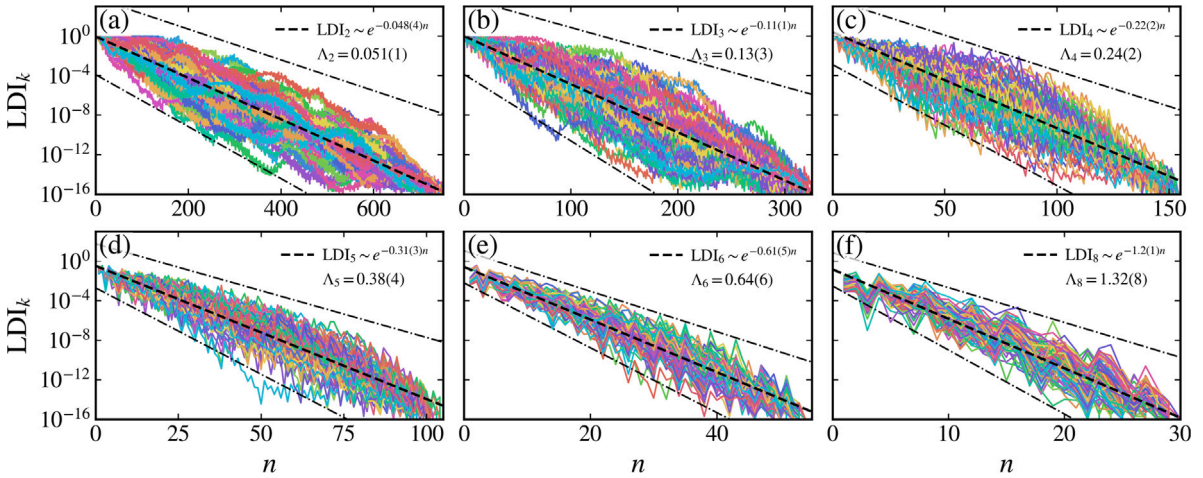

Fig. 5. LDI curves for a network of $N = 10$ identical logistic maps coupled in a ring topology (see Eq. (21)) with coupling strength $\sigma = 0.15$, coupling radius $r = 0.15$, and individual map bifurcation parameter $a = 3.8$. Panels (a)–(f) show LDI_2, LDI_3, LDI_4, LDI_5, LDI_6, and LDI_8, respectively, computed for 100 initial conditions randomly chosen within a distance of 10^{-3} from each other. (For interpretation of the references to color in this figure legend, the reader is referred to the web version of this article.)

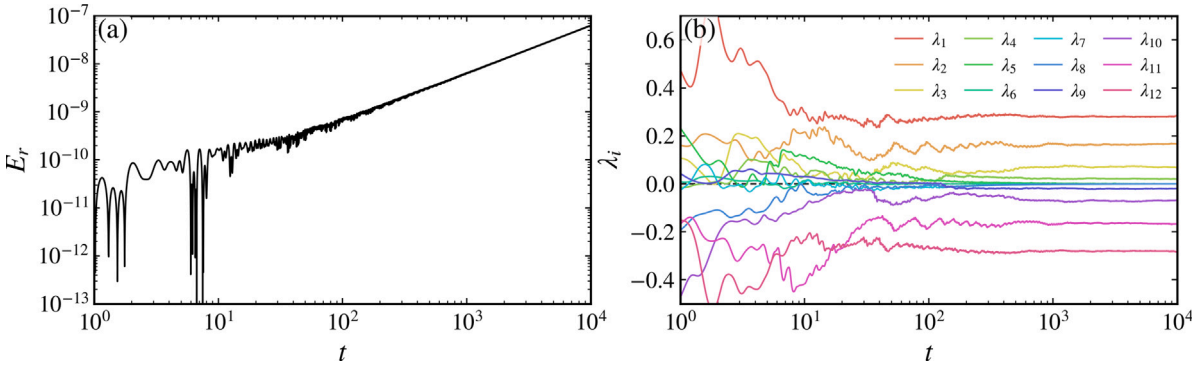

Fig. 6. Plot of the relative energy error and LEs in time for the FPU-β Hamiltonian in Eq. (22) with six particles and $\beta = 1.0$: (a) Relative energy error, $E_r = |E(t) - E_0|/E_0$ as a function of time. The equations of motion are integrated using the 4th-order Runge–Kutta method with a time step $\Delta t = 0.005$. (b) Evolution of the LEs for the same system. (For interpretation of the references to color in this figure legend, the reader is referred to the web version of this article.)

decay toward zero more rapidly as k gets closer to 10, yielding fewer data points and reducing the quality of the fit. This is so as the exponent in the exponential decay increases as k gets closer to 10. Therefore, we select $k = 2, 3, 4, 5, 6, 8$ as representative examples. For each LDI curve, we perform a best-fit analysis and plot the results together with the mean ± three standard deviations of all fits. We also compute the LEs for each initial condition and calculate their ensemble mean and standard deviations. Fig. 5 shows the LDI curves alongside the theoretical decay rates, given by $\Lambda_k = (k-1)\lambda_1 - \sum_{j=2}^{k} \lambda_j$. Again, the decay rates obtained from the LDI curves are in excellent agreement with the analytical expression obtained in Section 2. It is worth noting that the standard deviation for the numerically obtained LDI_8 is larger than for the smaller-k cases. This is a consequence of the rapid decay of LDI_8, which results in fewer data points for the fitting procedure. For comparison, LDI_2 takes approximately 700 iterations to drop below 10^{-16}, whereas LDI_8 reaches this threshold in about 30 iterations. Although this rapid decay leads to a poorer comparison with the analytical expression, it significantly reduces the computational cost for the detection of chaotic trajectories.

3.2. Continuous-time systems

To complement our analysis for discrete-time systems, we consider here a continuous-time system: the well-known Fermi–Pasta–Ulam (FPU) chain, a paradigmatic Hamiltonian system that can be extended to any number of degrees of freedom, to validate the analytical expression for the LDI given by Eq. (19). We focus on the FPU-β model, characterized by the Hamiltonian

$$H(\mathbf{p}, \mathbf{x}) = \frac{1}{2}\sum_{j=1}^{N} p_j^2 + \sum_{j=0}^{N}\left[\frac{1}{2}\left(x_{j+1} - x_j\right)^2 + \frac{1}{4}\beta\left(x_{j+1} - x_j\right)^4\right] = E, \tag{22}$$

where x_j denotes the displacement of the jth particle from its equilibrium position, with fixed boundary conditions (i.e., the particles with indices $j = 0$ and $j = N + 1$ remain stationary at all times). The p_j are the corresponding conjugate momenta, $\beta > 0$ is the nonlinear parameter, and E is the total, fixed energy of the system.

In our simulations, we set $\beta = 1.0$ and consider a chain of $N = 6$ particles, corresponding to 6 degrees of freedom and a system dimension of 12. All particles are initially at rest ($p_j = 0$) and at their equilibrium positions ($x_j = 0$), except for the second particle, which is displaced at $x_1 = 1$. This setup yields an initial energy of $E_0 = 1.5$. Since our focus is on the short-time evolution of the system, we integrate the equations of motion using the standard 4th-order Runge–Kutta scheme with a time step $\Delta t = 0.005$. To verify the accuracy of this numerical integration, we monitor the relative energy error,

$$E_r = \frac{\left|E(t) - E_0\right|}{E_0},$$

for a trajectory integrated up to $T = 10^4$ (see Fig. 6(a)). Even though the Runge–Kutta method is not a symplectic integrator, for this choice of time step, the energy error remains below 10^{-7} up to $T = 10^4$, providing an accurate description of the evolution of the system. Fig. 6(b) shows the evolution of the LEs. The system displays hyperchaotic behavior, and the sum of all exponents converges to $\sum_{j=1}^{12} \lambda_j \approx -3.88\times10^{-12}$, as expected for Hamiltonian systems, since they are volume-preserving in phase space. The fact that our numerical result remains extremely close to zero, thus, provides additional confirmation of the accuracy of our numerical integration.

To obtain the LDI decay rates, we consider 100 initial conditions randomly chosen within a distance of 10^{-2} from the reference initial condition, i.e., $x_1 = 0.01\epsilon$, where ϵ is a uniformly distributed random number in the interval $[0, 1)$. Similarly to the case of the network, we select $k = 2, 3, 4, 5, 6, 8$ as representative examples, and for each LDI curve, we calculate the best-fit to obtain the

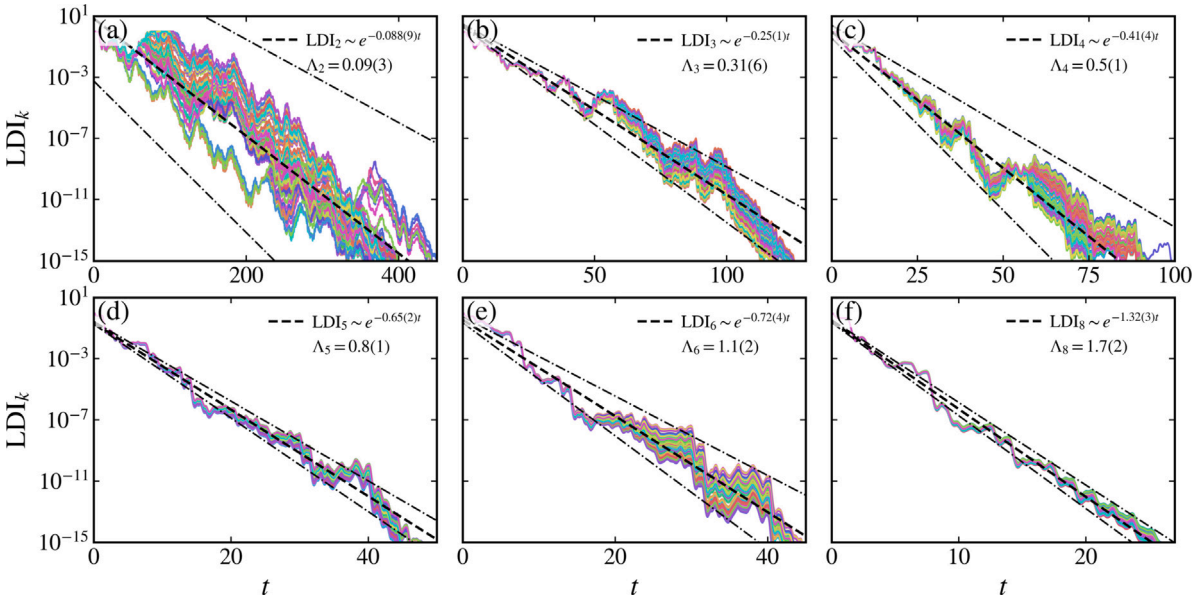

Fig. 7. LDI curves for the FPU chain with six particles and $\beta = 1.0$ (see Eq. (22)). Panels (a)–(f) show LDI_2, LDI_3, LDI_4, LDI_5, LDI_6, and LDI_8, respectively, computed for 100 initial conditions randomly perturbed within a distance of 10^{-2} from the reference configuration, as discussed in the text. (For interpretation of the references to color in this figure legend, the reader is referred to the web version of this article.)

corresponding decay rates. We then average the results over the 100 trajectories to obtain a representative LDI behavior. Fig. 7 shows the LDI curves for the aforementioned k values. The black dashed curves represent the average of all best-fit curves, while the black dash-dotted curves indicate the mean ± three standard deviations of the best-fit curves. Additionally, we compute the LEs for each initial condition for $T = 10^4$ and calculate their ensemble mean and standard deviations.

The decay rates obtained from the LDI curves are in good agreement with the theoretical predictions provided by Eq. (19), based on the LEs in Fig. 6(b). For $k = 2$, we find a decay rate of 0.088(9), which closely matches the corresponding analytical value $\Lambda_2 = \lambda_1 - \lambda_2 = 0.09(3)$. For larger k, the decay rates increase, reflecting the faster contraction of higher-order deviations: LDI_3 decays at 0.25(1) compared with $\Lambda_3 = 2\lambda_1 - \lambda_2 - \lambda_3 = 0.31(6)$, LDI_4 at 0.41(4) versus $\Lambda_4 = 3\lambda_1 - \sum_{j=2}^{4} \lambda_j = 0.5(1)$, and so on up to LDI_8, which decays at 1.32(3), with $\Lambda_8 = 1.7(2)$. While small discrepancies between numerical and theoretical values become more pronounced for larger k, these differences are expected due to the rapid decay of LDI_k, which reduces the number of points available for fitting and increases the standard deviation. Overall, the results confirm that the analytical expression $\Lambda_k = (k-1)\lambda_1 - \sum_{j=2}^{k} \lambda_j$ provides an accurate prediction for the decay of the LDI not only in discrete but also in continuous-time systems.

4. Analytical derivation of the decay rate of the Smaller Alignment Index for chaotic trajectories of discrete systems

In this section, we present an analytical derivation of the decay rate of SALI for chaotic trajectories of discrete-time systems and validate it numerically. While Moges et al. [41] have demonstrated recently that $GALI_2$ (i.e., SALI) can successfully detect stable fixed points in a three-dimensional generalization of the Hénon map, they also showed that GALI fails to distinguish among limit cycles, chaotic, and hyperchaotic attractors, as it decays exponentially in all these cases. In contrast, Skokos et al. [34,35] derived analytical expressions for the decay of SALI in Hamiltonian systems with N degrees of freedom. They showed that if the system has a single positive Lyapunov exponent (LE) with the second being zero, SALI decays as

$$\mathrm{SALI}(t) \propto e^{-\lambda_1 t}, \tag{23}$$

whereas it decays as

$$\mathrm{SALI}(t) \propto e^{-(\lambda_1 - \lambda_2)t} \tag{24}$$

if there are two positive LEs. While these results remain valid for d-dimensional continuous-time chaotic systems [41], there is a subtle difference when it comes to discrete-time chaotic systems. SALI in those systems exhibits a different behavior, which we derive and clarify next.

From Section 2, a normalized deviation vector, $\hat{\mathbf{d}}$, of a d-dimensional discrete-time system is given by Eq. (13). According to the SALI definition in Eq. (3), two such normalized vectors are required, that is $\hat{\mathbf{d}}_1$, $\hat{\mathbf{d}}_2$. Their sum and difference are given by

$$\begin{aligned}\hat{\mathbf{d}}_1 \pm \hat{\mathbf{d}}_2 = \frac{\mathbf{d}_1}{\|\mathbf{d}_1\|} \pm \frac{\mathbf{d}_2}{\|\mathbf{d}_2\|} &= \left(\mathrm{sgn}(c_1^{(1)}) \pm \mathrm{sgn}(c_1^{(2)})\right)\hat{\mathbf{w}}_1 + \sum_{i=2}^{d}\left(\frac{c_i^{(1)}}{\left|c_1^{(1)}\right|} \pm \frac{c_i^{(2)}}{\left|c_1^{(2)}\right|}\right)e^{-(\lambda_1-\lambda_i)n}\hat{\mathbf{w}}_i \\ &= C_{1,\pm}\hat{\mathbf{w}}_1 + \sum_{i=2}^{d} C_{2,i,\pm}e^{-(\lambda_1-\lambda_i)n}\hat{\mathbf{w}}_i.\end{aligned} \tag{25}$$

The norm is then given by

$$\left\|\frac{\mathbf{d}_1}{\|\mathbf{d}_1\|} \pm \frac{\mathbf{d}_2}{\|\mathbf{d}_2\|}\right\| = \left[C_{1,\pm}^2 + \sum_{i=2}^{d} C_{2,i,\pm}^2 e^{-2(\lambda_1-\lambda_i)n}\right]^{1/2}. \tag{26}$$

Since SALI is defined as the minimum over the $\pm$ combinations and $\min(C_{1,+}, C_{1,-}) = 0$, we have

$$\mathrm{SALI}(n) = \left[\sum_{i=2}^{d} C_i^2 e^{-2(\lambda_1-\lambda_i)n}\right]^{1/2},$$

with $C_i = \min(C_{2,i,+}, C_{2,i,-})$. Factoring out the dominant term $C_2 e^{-(\lambda_1-\lambda_2)n}$ gives

$$\mathrm{SALI}(n) = |C_2|e^{-(\lambda_1-\lambda_2)n}\left[1 + \sum_{i=3}^{d}\left(\frac{C_i}{C_2}\right)^2 e^{-2(\lambda_2-\lambda_i)n}\right]^{1/2}.$$

Since $e^{-2(\lambda_2-\lambda_i)n}$ $(i \geq 3)$ decays faster than $e^{-(\lambda_1-\lambda_2)n}$, the higher-order terms can be neglected, yielding

$$\mathrm{SALI}(n) \propto e^{-(\lambda_1-\lambda_2)n} \tag{27}$$

for discrete-time chaotic dynamics.

Interestingly, the authors in Ref. [35] showed that $\mathrm{GALI}_2 \propto \mathrm{SALI}$, and since we have shown here that $\mathrm{GALI}_k = \mathrm{LDI}_k$ (see Eq. (7)), including $k = 2$, the results in Fig. 5(a) for the network of $N = 10$ coupled logistic maps (see Eq. (21)) also apply to the case where LDI_2 is replaced by SALI. Hence, the results in Fig. 5(a) confirm numerically that Eq. (27) captures accurately the decay rate of SALI in the case where the first and the second LEs are positive, as corroborated by the plot of the LEs in Fig. 4(b).

Although Eq. (27) resembles Eqs. (23) and (24) mathematically, its interpretation is different when it comes to discrete-time systems: the decay rate depends on the two largest LEs, regardless of whether they are positive or negative. In contrast, the results in Ref. [34] assume continuous-time dynamics, where the second largest exponent is always non-negative for chaotic orbits. For example, in a two-dimensional area-preserving map, chaos is characterized by $\lambda_1 > 0$ and $\lambda_2 = -\lambda_1$. While the continuous-time assumption would incorrectly predict decay as in Eq. (23), the correct behavior follows Eq. (27), accounting for both exponents.

To demonstrate numerically Eq. (27), let us consider two examples of paradigmatic two-dimensional maps. The first one is Arnold's cat map, $\Phi : \mathbb{T}^2 \to \mathbb{T}^2$, where $\mathbb{T}^2 = \mathbb{R}^2/\mathbb{Z}^2$ denotes the two-dimensional torus

$$\Phi : \begin{cases} x_{n+1} = 2x_n + y_n \bmod 1, \\ y_{n+1} = x_n + y_n \bmod 1. \end{cases} \tag{28}$$

The system is a linear, hyperbolic, and mixing transformation with a positive largest LE. Its Jacobian matrix is constant, i.e., independent of the state variables, and is given by

$$D\Phi = \begin{pmatrix} 2 & 1 \\ 1 & 1 \end{pmatrix}.$$

Being symmetric, this matrix has real eigenvalues and mutually orthogonal eigenvectors. The map possesses a single fixed point at the origin (0,0). The eigenvalues of $D\Phi$ are given by

$$\mu_i = \frac{3 \pm \sqrt{5}}{2}.$$

Since $|\mu_1| > 1$ and $|\mu_2| < 1$, the origin is a hyperbolic (saddle) point. The eigenvector associated with μ_1 defines the unstable direction along which trajectories are exponentially stretched, while the eigenvector associated with μ_2 defines the stable direction along which trajectories are exponentially contracted.

Fig. 8(a) shows a rectangle of 20 000 randomly chosen initial conditions, and Fig. 8(b) shows how these initial conditions evolve for 100 iterations. The action of the map on the initial conditions is to stretch them exponentially along the unstable manifold and contract them exponentially along the stable manifold, with the modulo operation inducing a folding of phase space. The iterative application of this stretch–contract–fold mechanism produces a rapid dispersion of initially localized sets, ensuring strong mixing and the characteristic loss of memory of initial conditions observed in chaotic systems. In this setting, the LEs coincide with the logarithms of the eigenvalues of the Jacobian, i.e., $\lambda_i = \log \mu_i$, as the local dynamics everywhere is governed by the same linear transformation associated with the fixed point at the origin.

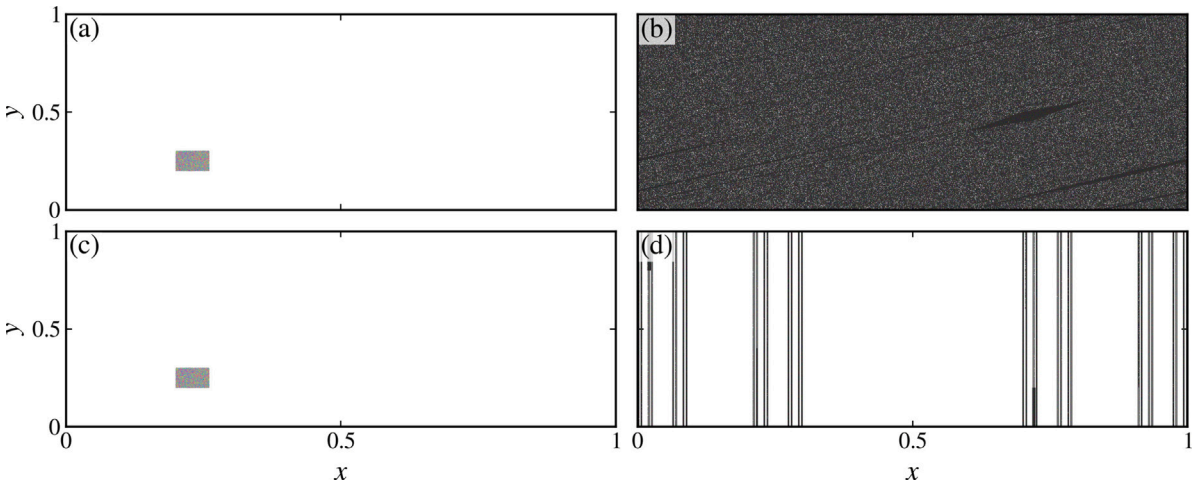

Fig. 8. The time evolution of a rectangle of initial conditions (see panels (a) and (c)) under the dynamics of (b) Arnold's cat map (see Eq. (28)) and (d) the baker map with $k = 0.3$ (see Eq. (29)).

The second map is the two-dimensional baker map [50]. It is a piecewise linear map defined as $\boldsymbol{\Phi} : \mathbf{x}_{n+1} = B(\mathbf{x}_n)$, where $\mathbf{x} = (x, y)$ and

$$B(x_n, y_n) = \begin{cases} B_-(x_n, y_n) = (kx_n, 2y_n), \\ B_+(x_n, y_n) = (1 + k(x_n - 1), 1 + 2(y_n - 1)), \end{cases} \tag{29}$$

where B_- and B_+ are valid for $y_n \leq 1/2$ and $y_n > 1/2$, respectively. Here the parameter $0 < k < 1$ controls the horizontal contraction and we consider $k = 0.3$. The action of the map is to stretch points vertically by a factor of 2 while simultaneously contracting them horizontally by a factor of k, relative to the origin for the lower half and to the point $(1, 1)$ for the upper half. Similar to Arnold's cat map, the Jacobian matrix of the baker map is constant

$$D\boldsymbol{\Phi} = \begin{pmatrix} k & 0 \\ 0 & 2 \end{pmatrix}.$$

The eigenvalues of the Jacobian matrix are easily obtained as $\mu_1 = 2$ and $\mu_2 = k$. The determinant of the Jacobian matrix is $\det(D\boldsymbol{\Phi}) = 2k$, which determines the phase space volume contraction rate: for $k = 0.5$ the map is area-preserving, for $k < 0.5$ dissipative, and for $k > 0.5$ expansive.

The baker map has two fixed points: the origin $(0, 0)$ and the point $(1, 1)$. Since $|\mu_1| > 1$ and $|\mu_2| < 1$, both of these points are hyperbolic. Their combined action produces the repeated stretching and contraction characteristic of chaotic motion. Consequently, the LEs of the map follow directly from the logarithms of the eigenvalues of the Jacobian matrix: $\lambda_1 = \log 2$ and $\lambda_2 = \log k$. Fig. 8(c) shows a rectangle of 20 000 randomly chosen initial conditions, and Fig. 8(d) shows the evolution of these initial conditions after 100 iterations.

Since the Jacobian matrices of both maps are constant, we analyze SALI using an ensemble of deviation matrices instead of initial conditions. For each deviation matrix, we first compute SALI over time. We then perform a best fit to this curve to extract its decay rate. This process is repeated for all deviation matrices in the ensemble. Finally, we average all the best-fit curves to obtain a representative SALI behavior. Fig. 9(a) shows the SALI curves for the cat map and Fig. 9(b) for the baker map, along with the average best-fit curve (black dashed line) and the mean ± three standard deviations of all best-fit curves (black dash-dotted lines). The decay rates obtained from the SALI curves are in excellent agreement with the theoretical prediction in Eq. (27). For the cat map, the decay rate is 1.92(1), closely matching the difference $\lambda_1 - \lambda_2 \approx 1.92485$ calculated from the Jacobian eigenvalues. Similarly, for the baker map, the SALI decay rate is 1.892(6), in good agreement with $\lambda_1 - \lambda_2 \approx 1.89712$. Therefore, these results confirm that the SALI decay is determined by the two largest LEs, even when the second one is negative.

5. Conclusions

In this work, we have analytically derived the formula for the decay rates of LDI for chaotic orbits and demonstrated that they are the same as those of GALI. The derivation was carried out using the Singular Value Decomposition (SVD) of the matrix formed by the deviation vectors, which provides a direct connection between the decay of LDI and the growth rates of the singular values. This linear-algebraic formulation offers a more transparent route to the decay behavior compared to the wedge-product interpretation of GALI and applies in the same way to both discrete- and continuous-time systems. While previous studies validated GALI [35] and LDI [40] in continuous-time Hamiltonian systems, here we have provided a comprehensive verification for discrete-time systems, including both low- and high-dimensional systems. Recently, Moges et al. [41] applied GALI to a three-dimensional generalization

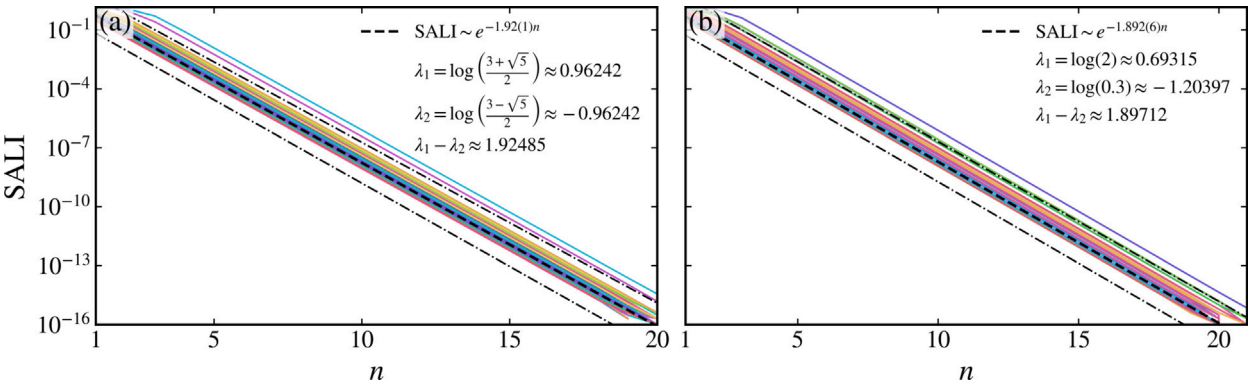

Fig. 9. Time evolution of the SALI for 100 randomly chosen deviation vectors: (a) Arnold's cat map [Eq. (28)] and (b) the baker map with $k = 0.3$ [Eq. (29)]. Each color represents a different deviation vector. The black dashed lines indicate the average SALI decay, while the black dash-dotted lines show the average ± three standard deviations from the mean. (For interpretation of the references to color in this figure legend, the reader is referred to the web version of this article.)

of the Hénon map. They demonstrated that $GALI_2$ reliably detects stable fixed points and that $GALI_2$ and $GALI_3$ decay exponentially. Here, our focus has been on establishing the equivalence of the decay rates of LDI and GALI and on confirming analytically and numerically their validity, given in Eq. (19) for both discrete-time and continuous-time systems.

Moreover, we have provided an analytical formula for the decay rate of SALI for discrete-time chaotic systems. While earlier derivations were valid for continuous-time dynamics [34], the decay rate therein underestimated the decay rate in discrete-time systems. Our analysis for chaotic discrete-time systems shows that SALI decays according to the difference of the two largest LEs, even when the second exponent is negative. We have confirmed numerically our analytical results for two paradigmatic two-dimensional chaotic maps, Arnold's cat map and baker map.

Interestingly, the LDI method can, in principle, be employed to reconstruct the entire Lyapunov spectrum. Starting from the largest LE, λ_1, which is generally easier to estimate, one could determine λ_2 from the decay rate of LDI_2, then λ_3 from LDI_3, and so on and so forth. However, this procedure accumulates numerical errors from the best-fits of successive LDI curves and requires computing all indices from LDI_2 up to LDI_d, where d is the dimension of the system. As we have shown here, the best-fit of higher order LDI is less accurate due to its rapid decay, and consequently, there are fewer points available to compute the best-fit lines. As a result, it is computationally more demanding and less accurate than the classical Benettin et al. [3] algorithm based on QR decomposition. For these reasons, we have not pursued or displayed such results in this paper.

Overall, our results provide a unified analytical and numerical framework for understanding the behavior of the decay rates of LDI, GALI, and SALI in both discrete- and continuous-time chaotic systems. This framework enables efficient chaos detection and a deeper understanding of phase-space structure in low- and high-dimensional systems, and can be readily applied to a wide range of complex dynamical systems.

CRediT authorship contribution statement

Matheus Rolim Sales: Writing – review & editing, Writing – original draft, Visualization, Validation, Software, Methodology, Investigation, Formal analysis, Data curation, Conceptualization. **Edson Denis Leonel:** Writing – review & editing, Writing – original draft, Visualization, Validation, Methodology, Investigation, Formal analysis, Data curation, Conceptualization. **Chris G. Antonopoulos:** Writing – review & editing, Writing – original draft, Visualization, Validation, Supervision, Methodology, Investigation, Formal analysis, Data curation, Conceptualization.

Code availability

The source code to reproduce the results reported in this paper is freely available in the GitHub repository in Ref. [51].

Declaration of competing interest

The authors declare that they have no known competing financial interests or personal relationships that could have appeared to influence the work reported in this paper.

Acknowledgments

This work was supported by the São Paulo Research Foundation (FAPESP, Brazil), under Grant Nos. 2019/14038-6, 2021/09519-5, 2023/08698-9 and 2024/09208-8, by the National Council for Scientific and Technological Development (CNPq, Brazil), under Grant Nos. 301318/2019-0 and 304398/2023-3.

Table A.1
Wall times for computing LDI_k for the coupled logistic map network introduced in Section 3.1 and defined in Eq. (21), with system size $N = 10$. For each value of k, the wall time was obtained from 10 independent runs, and the reported values correspond to the sample mean and standard deviation.

k	2	10	50	100	250	500
Time	30.7 s ± 3.78 s	1.88 s ± 336 ms	531 ms ± 118 ms	318 ms ± 96.3 ms	293 ms ± 35.3 ms	576 ms ± 59 ms

Appendix. Computational performance

In this section, we compare the computational cost of computing the Lyapunov exponents using the standard QR-based method [3] with the cost of evaluating the LDI_k indicator via the SVD-based procedure. All benchmarks were performed using the coupled logistic map network defined in Eq. (21) with $N = 500$ nodes and a coupling strength and radius of $(\sigma, r) = (0.15, 0.05)$. These benchmarks were obtained in a MacBook Air equipped with an Apple M4 chip, featuring a 10-core CPU. For each method, we carried out 10 independent simulations, each consisting of 1.5×10^6 iterations after discarding an initial transient of 0.5×10^6 steps. We obtain a mean wall-clock time of $53.1\,\mathrm{s} \pm 3.32\,\mathrm{s}$ for the maximum Lyapunov exponent only across the 10 realizations.

Table A.1 reports the corresponding wall times for LDI_k for selected values of k. In contrast to the Lyapunov exponent calculation, the LDI_k computation is substantially faster, typically by about two orders of magnitude. This difference is due to the fact that the LDI_k indicator allows for early termination: we are not concerned with the precise asymptotic value of LDI_k, but rather with how it decays. Chaotic trajectories exhibit an exponential decay, whereas regular trajectories decay algebraically. Therefore, once LDI_k falls below a threshold (here chosen as 10^{-16}), the trajectory's nature is already determined, and the computation is stopped.

Importantly, this early termination applies only to the LDI calculation. The Lyapunov exponent computation, on the other hand, requires performing QR orthonormalization at every iteration step up to the full simulation time, regardless of whether the trajectory is chaotic or regular. As a result, the LDI approach incurs far fewer tangent-space updates and avoids the repeated re-orthogonalization steps inherent in the Lyapunov exponent algorithm. This makes LDI_k particularly advantageous for long simulations and in large-dimensional systems where the cost of QR-based propagation is significant.

Data availability

The source code to reproduce the results reported in this paper is freely available in the GitHub repository in Ref. [51].

References

[1] Lorenz EN. Deterministic nonperiodic flow. J Atmospheric Sci 1963;20(2):130–41.
[2] Shimada I, Nagashima T. A numerical approach to ergodic problem of dissipative dynamical systems. Progr Theoret Phys 1979;61:1605–16.
[3] Benettin G, Galgani L, Giorgilli A, Strelcyn J-M. Lyapunov characteristic exponents for smooth dynamical systems and for Hamiltonian systems; a method for computing all of them. Part 1: Theory. Meccanica 1980;15:9–20.
[4] Wolf A, Swift JB, Swinney HL, Vastano JA. Determining Lyapunov exponents from a time series. Phys D 1985;16(3):285–317.
[5] Eckmann JP, Ruelle D. Ergodic theory of chaos and strange attractors. Rev Modern Phys 1985;57:617–56.
[6] Froeschlé C, Lega E, Gonczi R. Fast Lyapunov indicators. Application to asteroidal motion. Celest Mech Dyn Astron 1997;67(1):41–62.
[7] Froeschlé C, Gonczi R, Lega E. The fast lyapunov indicator: a simple tool to detect weak chaos. application to the structure of the main asteroidal belt. Planet Space Sci 1997;45(7):881–6, Asteroids, Comets, Meteors 1996 - II.
[8] Barrio R. Sensitivity tools vs. Poincaré sections. Chaos Solitons Fractals 2005;25(3):711–26.
[9] Sándor Z, Érdi B, Efthymiopoulos C. The phase space structure around L4 in the restricted three-body problem. Celest Mech Dyn Astron 2000;78(1):113–23.
[10] Sándor Z, Érdi B, Széll A, Funk B. The relative Lyapunov indicator: An efficient method of chaos detection. Celest Mech Dyn Astron 2004;90(1):127–38.
[11] Cincotta PM, Simó C. Simple tools to study global dynamics in non-axisymmetric galactic potentials – i. Astron Astrophys Suppl Ser 2000;147(2):205–28.
[12] Cincotta PM, Giordano CM, Simó C. Phase space structure of multi-dimensional systems by means of the mean exponential growth factor of nearby orbits. Phys D 2003;182(3):151–78.
[13] Gottwald GA, Melbourne I. A new test for chaos in deterministic systems. Proc R Soc Lond A 2004;460(2042):603–11.
[14] Szezech JD, Schelin AB, Caldas IL, Lopes SR, Morrison PJ, Viana RL. Finite-time rotation number: A fast indicator for chaotic dynamical structures. Phys Lett A 2013;377(6):452–6.
[15] Levnajić Z, Mezić I. Ergodic theory and visualization. I. Mesochronic plots for visualization of ergodic partition and invariant sets. Chaos 2010;20:033114.
[16] Levnajić Z, Mezić I. Ergodic theory and visualization. II. Fourier mesochronic plots visualize (quasi)periodic sets. Chaos 2015;25:053105.
[17] Das S, Dock CB, Saiki Y, Salgado-Flores M, Sander E, Wu J, Yorke JA. Measuring quasiperiodicity. EPL (Europhys Lett) 2016;114:40005.
[18] Das S, Saiki Y, Sander E, Yorke JA. Quantitative quasiperiodicity. Nonlinearity 2017;30:4111–40.
[19] Das S, Yorke JA. Super convergence of ergodic averages for quasiperiodic orbits. Nonlinearity 2018;31:491–501.
[20] Sander E, Meiss JD. Birkhoff averages and rotational invariant circles for area-preserving maps. Phys D 2020;411:132569.
[21] Meiss JD, Sander E. Birkhoff averages and the breakdown of invariant tori in volume-preserving maps. Phys D 2021;428:133048.
[22] Sales MR, Mugnaine M, Viana RL, Caldas IL, Szezech JD. Unpredictability in Hamiltonian systems with a hierarchical phase space. Phys Lett A 2022;431:127991.
[23] Duignan N, Meiss JD. Distinguishing between regular and chaotic orbits of flows by the weighted birkhoff average. Phys D 2023;449:133749.
[24] Trulla LL, Giuliani A, Zbilut JP, Webber CL. Recurrence quantification analysis of the logistic equation with transients. Phys Lett A 1996;223(4):255–60.
[25] Marwan N, Wessel N, Meyerfeldt U, Schirdewan A, Kurths J. Recurrence-plot-based measures of complexity and their application to heart-rate-variability data. Phys Rev E 2002;66:026702.
[26] Zou Y, Pazó D, Romano MC, Thiel M, Kurths J. Distinguishing quasiperiodic dynamics from chaos in short-time series. Phys Rev E 2007;76:016210.
[27] Zou Y, Thiel M, Romano MC, Kurths J. Characterization of stickiness by means of recurrence. Chaos 2007;17:043101.

[28] Ngamga EJ, Senthilkumar DV, Kurths J. Dynamics between order and chaos revisited. Eur Phys J Spec Top 2010;191(1):15–27.
[29] Eroglu D, Peron TKD, Marwan N, Rodrigues FA, Costa LdF, Sebek M, Kiss IZ, Kurths J. Entropy of weighted recurrence plots. Phys Rev E 2014;90:042919.
[30] Sales MR, Mugnaine M, Szezech J, José D, Viana RL, Caldas IL, Marwan N, Kurths J. Stickiness and recurrence plots: An entropy-based approach. Chaos 2023;33:033140.
[31] Gabrick EC, Sales MR, Sayari E, Trobia J, Lenzi EK, Borges FS, Szezech Jr J, Iarosz KC, Viana RL, Caldas I, Batista AM. Fractional dynamics and recurrence analysis in cancer model. Braz J Phys 2023;53(6):145.
[32] Skokos C. Alignment indices: a new, simple method for determining the ordered or chaotic nature of orbits. J Phys A: Math Gen 2001;34:10029.
[33] Skokos C, Antonopoulos C, Bountis TC, Vrahatis MN. Smaller alignment index (SALI): determining the ordered or chaotic nature of orbits in conservative dynamical systems. In: Libration point orbits and applications. World Scientific; 2003, p. 653–64.
[34] Skokos C, Antonopoulos C, Bountis TC, Vrahatis MN. Detecting order and chaos in Hamiltonian systems by the SALI method. J Phys A: Math Gen 2004;37:6269–84.
[35] Skokos C, Bountis TC, Antonopoulos C. Geometrical properties of local dynamics in Hamiltonian systems: The generalized alignment index (GALI) method. Phys D 2007;231:30–54.
[36] Skokos C, Bountis T, Antonopoulos C. Detecting chaos, determining the dimensions of tori and predicting slow diffusion in fermi–pasta–ulam lattices by the generalized alignment index method. Eur Phys J Spec Top 2008;165(1):5–14.
[37] Manos T, Skokos C, Antonopoulos C. Probing the local dynamics of periodic orbits by the generalized alignment index (GALI) method. Int J Bifurc Chaos 2012;22(09):1250218.
[38] Skokos CH, Manos T. The smaller (SALI) and the generalized (GALI) alignment indices: efficient methods of chaos detection. Berlin, Heidelberg: Springer Berlin Heidelberg; 2016, p. 129–81.
[39] Many Manda B, Hillebrand M, Skokos C. Efficient detection of chaos through the computation of the generalized alignment index (GALI) by the multi-particle method. Commun Nonlinear Sci Numer Simul 2025;143:108635.
[40] Antonopoulos C, Bountis T. Detecting order and chaos by the linear dependence index (LDI) method. Romai J 2006;2(2):1–13.
[41] Moges HT, Manos T, Racoveanu O, Skokos C. On the behavior of the generalized alignment index (GALI) method for dissipative systems. Int J Bifurc Chaos 2025;35.
[42] Alligood KT, Sauer TD, Yorke JA. Chaos: an introduction to dynamical systems. Textbooks in mathematical sciences, 1st corr. ed.. New York: Springer–Verlag; 1996.
[43] Ott E. Chaos in dynamical systems. 2nd ed.. Cambridge University Press; 2002.
[44] Kato T. Perturbation theory for linear operators. Classics in mathematics, 2nd ed.. Berlin, Heidelberg: Springer; 2012.
[45] Golub GH, Van Loan CF. Matrix computations. 4th ed.. Philadelphia, PA: Johns Hopkins University Press; 2013.
[46] Higham NJ. Accuracy and stability of numerical algorithms. 2nd ed.. Society for Industrial and Applied Mathematics; 2002.
[47] Sales MR, de Souza LC, Borin D, Mugnaine M, Szezech JD, Viana RL, Caldas IL, Leonel ED, Antonopoulos CG. Pynamicalsys: A Python toolkit for the analysis of dynamical systems. Chaos Solitons Fractals 2025;201:117269.
[48] Gonchenko SV, Ovsyannikov II, Simó C, Turaev D. Three-dimensional Hénon-like maps and wild Lorenz-like attractors. Int J Bifurc Chaos 2005;15(11):3493–508.
[49] Omelchenko I, Maistrenko Y, Hövel P, Schöll E. Loss of coherence in dynamical networks: Spatial chaos and Chimera states. Phys Rev Lett 2011;106:234102.
[50] Tél T, Gruiz M. Chaotic dynamics: an introduction based on classical mechanics. Cambridge University Press; 2006.
[51] Rolim Sales M. mrolims-publications/alignment-indices-chaotic. 2025.